Photogenerated electron modulation to dominantly induce efficient 2,4-dichlorophenol degradation on BiOBr nanoplates with different phosphate modification

Shuangying Chen, Rui Yan[*,1], Xuliang Zhang, Kang Hu, Zhijun Li, Muhammad Humayun, Yang Qu, Liqiang Jing[*]

Key Laboratory of Functional Inorganic Materials Chemistry (Heilongjiang University), Ministry of Education, School of Chemistry and Materials Science, International Joint Research Center for Catalytic Technology, Harbin 150080, PR China

ABSTRACT

It is highly desired to modulate the photogenerated electrons for efficient photocatalysis on BiOBr to degrade pollutants. Herein, BiOBr nanoplates have been successfully modified respectively by the molecular hydrogen phosphate groups and the bismuth phosphate nanoparticles. It is clearly demonstrated mainly based on the steady-state- and transient-state- surface photovoltage responses that the two modified phosphates with proper amounts could greatly increase the separation and the lifetime of photogenerated charges, especially for the bismuth phosphate one, leading to the obviously improved photocatalytic activities for degrading pollutants, like 2,4-dichlorophenol (2,4-DCP). Interestingly, it is confirmed that the enhanced charge separation is attributed to the photogenerated electron modulation, respectively by the modified hydrogen phosphate to enhance the adsorption of O_2 so as to promote the electrons captured and by the modified bismuth phosphate to collect the excited high-energy-level electrons. Moreover, it is expectedly demonstrated by means of the radical-trapping experiments that the formed $^{\bullet}O_2^-$ species as the electron-modulated direct products could dominate the photocatalytic degradation of 2,4-DCP. Furthermore, the possible degradation mechanism related to $^{\bullet}O_2^-$ attack is proposed through the detected main intermediates, like parachlorophenol superoxide radical, and mineralized chloride.

© 2017 Elsevier B.V. All rights reserved.

1. Introduction

Chlorophenols, as the typical degradation-resistant organic pollutants, have been included as priority pollutants by the United States Environmental Protection Agency [1]. Even a low concentration of chlorophenols would cause severe damage to the organisms and environment [2,3]. Among them, 2,4-DCP is regarded as one of the most typical chlorophenols, mainly due to its wide application as pesticides, sanitizers, preservatives, germicides and herbicides [4–6]. Therefore, great efforts have been made to remove the 2,4-DCP from the polluted water bodies. Currently, the photocatalytic technique is considered as one of the most promising techniques to degrade pollutants owing to its effective, low-cost and environmentally friendly [7]. Noteworthily, the photocatalytic degradation of chlorophenols has been well studied [8,9]. However, the low photocatalytic efficiency and the ambiguous photodegradation mechanisms still greatly limit the practical application of photocatalytic techniques.

Bismuth oxyhalides BiOX (X = Cl, Br, I) as potential photocatalysts are favored due to their indirect transition band gap and layered structure. The excited electrons of BiOX travel a certain k-space distance from the valence band (VB) that reduces the recombination probability of photogenerated electron-hole pairs [10,11]. Moreover, the layered structure provides enough space to polarize the related atoms and orbitals, resulting in the appearance of the internal static electric fields perpendicular to the $[Bi_2O_2]$ slabs and halogen anionic slabs in BiOX. This leads to the excellent photocatalytic activities [12,13]. As a typical bismuth oxyhalides, besides possessing the common advantages, BiOBr is much favorable owing to its good stability and narrow band gap for visible-light response [14–16]. Therefore, BiOBr has been regarded as a potential candidate for effective degradation of pollutants.

In general, O_2 is a kind of oxidant, and the adsorbed O_2 on semiconductors can capture the photogenerated electrons to prevent the accumulation of negative charges, leading to the promoted photogenerated charge separation. Thus, it is of great significance to improve the O_2 adsorption capacity of semiconductor photocatalysts [17–20]. Noticeably, the conduction band (CB) bottom and valence band (VB) top of BiOBr are located at +0.2 eV and +3.0 eV, respectively, vs SHE [21]. This indicates that it is easy for the photogenerated holes to induce the oxidation reactions with H_2O and organic pollutants [22]. In contrast, it is not feasible for the photogenerated electrons to be captured by the adsorbed O_2 thermodynamically since the potential of O_2 reduction is at about 0 eV [21,23]. Based on the above analysis, it is suggested that the electron modulation is vital to efficient photocatalysis on BiOBr. However, the relative issues are always neglected.

It is considered that the photogenerated electrons of BiOBr could be modulated by the adsorbed O_2, and hence it is a feasible strategy to enhance the charge separation by promoting the adsorption of O_2 [17–20]. However, it seems to be neglected for BiOBr. In our previous works, it is clearly shown that the hydrogen phosphate modification of TiO_2 and Fe_2O_3 could promote the adsorption of O_2 so as to enhance the charge separation and then to improve the photocatalytic activities for degrading pollutants [24,25]. Therefore, it is meaningful to carry out the hydrogen phosphate modification on BiOBr for effective degradation of pollutants, since related works have not been reported up to date.

In addition, it is a great challenge for BiOBr to overcome the natural limitation from its positive CB bottom position. Actually, the generated high-energy-level (HEL) electrons above 0 eV under light irradiation should possess strong capacity to induce reduction reactions with the adsorbed O_2. However, these HEL electrons would quickly relax to the CB bottom within ∼ps timescale so as to greatly lose potential energy. Hence, it is necessary to develop a reasonable strategy to utilize the excited HEL electrons for efficiently improving the photocatalytic activities of BiOBr. Unfortunately, few related works have been studied for the BiOBr photocatalyst.

In our previous works [26–28], it has been shown that the photogenerated charge separation of visible-light responsive oxides, such as Fe_2O_3, $BiVO_4$ and $BiFeO_3$, could be enhanced by coupling wide-bandgap oxides, like TiO_2 and ZnO, leading to the greatly improved visible-light photocatalytic activities. And also, it is suggested that the enhanced charge separation is attributed to the visible-light excited HEL electron transfer. Naturally expected, this strategy might apply to enhance the charge separation of BiOBr by coupling a wide-bandgap semiconductor with a suitable CB bottom level to achieve the photocatalytic activity enhancement. Similar to TiO_2, the widely reported $BiPO_4$ possesses a high CB bottom level (−0.16 eV), which is adaptable to couple with the BiOBr to realize effective utilization of the HEL electrons [29–31]. However, the hybrid photocatalyst by the combination of BiOBr and $BiPO_4$ has seldom been studied. Based on the above strategy, it is much meaningful to construct a heterojunctional nanocomposite by depositing in situ nanocrystalline $BiPO_4$ on the surfaces of BiOBr for efficient photocatalysis.

Herein, we have successfully developed two methods to modulate the photogenerated electrons for efficient photocatalysis over BiOBr nanoplates to degrade chlorophenols, including the promoted adsorption of O_2 by the modified hydrogen phosphate and the introduced HEL platform by the modified bismuth phosphate, especially for the later. Moreover, the vital role of the formed $\cdot O_2{}^-$ in the degradation of 2,4-DCP has been confirmed. Furthermore, the 2,4-DCP degradation mechanism involving $\cdot O_2{}^-$ attack has been studied rigorously based on the detected main intermediates and the mineralized Cl^-. This work will help us to well understand the importance to modulate the photogenerated electrons for efficient photocatalysis, and also provide a feasible strategy to improve the photocatalytic activities of BiOX for environmental remediation.

2. Experimental

2.1. Reagents

All the reagents were of analytical grade and used as received without further purification. Deionized water was used throughout.

2.2. Synthesis of materials

BiOBr nanoplates were prepared by a hydrothermal method as follows [32]. In a typical experiment, 2 mmol of $Bi(NO_3)_3 \cdot 5H_2O$ was dissolved in 18 mL of HNO_3 solution (1 mol L^{-1}), under vigorous stirring for 10 min, followed by ultrasonication for 10 min, which is labeled as solution A. Then, 2 mmol of KBr was dissolved in 12 mL of HNO_3 solution (1 mol L^{-1}), which was kept under stirring for 10 min and labeled as solution B. The solution B was added dropwise to solution A, which was kept under stirring for 30 min. Then, the resulting mixture was transferred into a 50 mL of teflon-lined stainless steel autoclave to carry out a hydrothermal treatment at 160 °C for 6 h. After cooling to room temperature naturally, the yellow product was centrifuged and washed several times with deionized water, followed by absolute ethanol, and finally dried at 80 °C overnight.

To modify BiOBr with different phosphates, a certain amount of the resulting BiOBr was added to the planned concentration of different phosphate solution in a glass container under stirring for 1.5 h. Subsequently, the mixture was sonicated for 10 min. Then, the mixture was naturally precipitated and removed the supernatant. After drying at 80 °C for 24 h, the modified BiOBr samples were obtained, respectively denoted as XP-BiOBr and XPP-BiOBr, in which X is the mole ratio percentage of used phosphate to BiOBr, and P and PP respectively represent hydrogen phosphate and sodium pyrophosphate.

2.3. Characterization of materials

The X-ray powder diffraction (XRD) patterns of the samples were measured with a Bruker D8 Advance diffractometer, using CuKα radiation. The UV/Vis diffuse reflectance spectra (UV/Vis DRS) of the samples were measured with a Model Shimadzu UV2550 spectrophotometer, using $BaSO_4$ as a reference. The Fourier-transform infrared (FTIR) spectra of the samples were collected with a Bruker Equinox 55 Spectrometer, using KBr as diluents. The X-ray photoelectron spectroscopy (XPS) technique was used to detect the surface composition and elemental chemical state of the samples, by using a Model VG ESCALAB apparatus with Mg K X-ray source, and the binding energies were calibrated with respect to the signal for adventitious carbon (binding energy = 284.6 eV). Transmission electron microscopy (TEM) images of various samples were taken by a JEOL JEM-2010 electron microscope with an acceleration voltage of 200 kV. The steady-state surface photovoltage spectroscopy (SS-SPS) measurement of the samples was carried out with a home-built apparatus, the signal was collected by a lock-in amplier (SR830) synchronized with a light chopper (SR540). The mono-chromatic light was obtained by passing light from a 500W xenon lamp (CHF XQ500W) through a double prism monochromator (SBP300). The transient-state surface photovoltage (TS-SPV) measurement was performed in air atmosphere and at room temperature. The samples were excited by a radiation pulse of 355 nm with 10 ns width from a second harmonic Nd: YAG laser (Lab-130-10H, Newport, Co.). The signal was amplified with a preamplifier

and then registered by a 1 GHz digital phosphor oscilloscope (DPO 4104B, Tektronix) [33].

2.4. Evaluation for O_2 temperature-programmed desorption

The temperature-programmed desorption (TPD) curves of O_2 were measured with a home-built flow apparatus. The typical method is as follows, 50 mg of sample powder was pretreated at 270 °C for 0.5 h with an ultra-high-purity Helium (He) flow. After that, the system was cooled to room temperature and then the sample was blown continuously with O_2 for 90 min at 30 °C. Subsequently, He was passed through the system to remove O_2. Finally, the O_2-TPD profiles of the samples were recorded by increasing the temperature from 30 to 550 °C at a heating rate of 10 °C min^{-1} under the flow of He. The desorbed O_2 was analyzed by a gas chromatograph (GC-2014, Shimadzu) with a TCD detector.

2.5. Analysis of produced hydroxyl radical amount

0.02 g BiOBr powder was dispersed in 50 mL coumarin aqueous solution (0.001 M) in a beaker. Prior to irradiation, the reactor was magnetically stirred for 10 min to attain an adsorption-desorption equilibrium. After irradiation for 1 h with a 150 W GYZ220 high-pressure Xenon lamp (made in China), the sample was centrifuged, and then a certain volume of solution was transferred into a Pyrex glass cell for the fluorescence measurement of 7-hydroxycoumarin at 332 nm excitation wavelength with an emission wavelength at 456 nm through a spectrofluorometer (Perkin-Elmer LS55). For the single wavelength experiments, we used the CEL-LED 100W lamp with 405 nm, 385 nm and 365 nm wavelengths to irradiate for 1 h.

2.6. Electrochemistry (EC) measurements

Firstly, we prepared the electrode films of the samples according to our previous work [24]. Then, the electrochemical experiments were performed in a three-electrode cell with a Platinum wire (99.9%) as the counter electrode, a saturated KCl Ag/AgCl electrode as the reference electrode, the prepared film electrodes as the working electrode, and the 0.5 M NaClO$_4$ solution as the electrolyte. Subsequently, high-purity O_2 gas was used to bubble through the electrolyte before and during the experiments. The electrochemical O_2 reduction experiments were measured in dark. Applied potentials were controlled by a commercial computer-controlled potentiostat (AUTOLABPG STAT 101).

2.7. Evaluation of photocatalytic activities for degrading pollutants

The activities of the samples were evaluated by photodegradation of phenol, 2,4-DCP and rhodamine B using a 150 W xenon lamp (GYZ220). For phenol degradation, the photocatalyst powder (0.2 g) and phenol solution (50 mL, 10 mg L^{-1}) were mixed in a photochemical glass reactor under magnetic stirring at the room temperature and standard pressure. Prior to irradiation, the reactive system was stirred magnetically in dark for 30 min to reach the adsorption-desorption equilibrium. After photocatalytic reaction for 1 h, the solution was centrifuged and the concentration was measured with a Shimadzu UV-2550 spectrophotometer through the 4-aminoantipyrine spectrophotometric method at the characteristic optical absorption of 510 nm. For 2,4-DCP degradation, the experiments were performed in a similar way to the photocatalytic degradation of phenol, 0.2 g power and 2,4-DCP solution (50 mL, 10 mg L^{-1}) were used. The concentration of 2,4-DCP was measured at the characteristic optical absorption of 285 nm. For the photocatalytic degradation of rhodamine B, the powder (0.02 g) and

rhodamine B solution (100 mL, 15 mg L^{-1}) were used, and the solution was stirrer for 0.5 h in dark, in order to reach the adsorption equilibrium. Then, the solution was kept under stirring and irradiated for 1.5 h, the solution was centrifuged and the concentration of RhB was analyzed at intervals of 0.5 h by means of the characteristic optical absorption at 553 nm with a Model Shimadzu UV2550 spectrophotometer.

2.8. Measurements of produced intermediates and Cl^- amount

The intermediates formed during the photodegradation of 2,4-DCP were detected. In a typical experiment, 0.3 g 0.3PP-BiOBr was mixed with 80 mL of 10 mg L^{-1} 2,4-DCP solution by a magnetic stirrer for 0.5 h in dark, in order to keep the reactive system uniform and adsorption equilibrium. After that, the system begins to be irradiated with GYZ220 for 2.5 h. Each 0.5 h interval, a planed amount of the solution was centrifuged. The intermediates were analyzed with Agilent liquid chromatography tandem mass spectrometry (6410MS, USA) technique. The fragments of the main reaction intermediate were analyzed through scan mode. To detect the produced Cl^- amount, a Thermor Dionex ICS-600 IC equipped with an isocratic pump and a dialysis system was used. A mixture of Na$_2$CO$_3$ (4.5 mmol L^{-1}) and NaHCO$_3$ (8.0 mmol L^{-1}) aqueous solutions was taken as the mobile phase. The eluent flow rate was fixed at 0.8 mL/min. The samples were injected by using a 100 µL PEEK loop. Duplicate runs were performed on chromotography columns (Ion Pac AS23 4.0 × 250 mm). An AERS 500 eluent suppressor was used in an auto-recycle mode before the detector. Data was acquired and analyzed by Chromeleon V6.8 chromatography data software. The standard stock solution of chloride anions (1000 µg/mL) was purchased by Central Iron And Steel Research Institute. Standard solutions of chloride anions (i.e. 0.05, 0.10, 0.25, 0.50, 0.75 and 1.0 mg/L) were prepared, and the obtained linear equation: y = 2.760c, with the correlation coefficient of 0.9991.

3. Results and discussion

3.1. Effects of modification with hydrogen phosphate

The XRD measurements are performed to determine the crystalline structure and phase purity of BiOBr and XP-BiOBr, and the corresponding XRD patterns are shown in SI-Fig. 1A. The XRD patterns of BiOBr exhibit six major peaks, which are respectively indexed to the (001), (101), (102), (110), (200) and (212) planes of tetragonal BiOBr (JCPDS File No. 09-0393) [34]. No characteristic peaks of other phases or impurities are observed, indicating the high purity of resulting BiOBr. It is noticed that the crystal phase of BiOBr is not changed after the modification with hydrogen phosphate. Meanwhile, no other impurities are detected. Moreover, the typical diffuse reflectance spectra of BiOBr and XP-BiOBr are shown in SI-Fig. 1B. The calculated energy band gap of BiOBr is approximately 2.8 eV, based on the widely accepted equation Eg = 1240/λ [35]. The optical absorption of BiOBr is unchanged after the modification with hydrogen phosphate. To further investigate the chemical bonding between the modifier and BiOBr, the FT-IR spectra are obtained as shown in SI-Fig. 1C. The strong peaks at low frequency (about 500 cm^{-1}) are attributed to the vibration of Bi–O bonds [36]. Noteworthily, a new peak appears at about 1020 cm^{-1} for XP-BiOBr, which is ascribed to the phosphate groups [25]. Thus, it is confirmed that the phosphate groups have been successfully modified on the surfaces of BiOBr nanoplates.

The steady-state surface photovoltage spectroscopy (SS-SPS) is a reliable and sensitive technique used to explore the photogenerated charge properties of solid semiconductors [37,38]. It is commonly accepted that the SS-SPS responses of nanosized
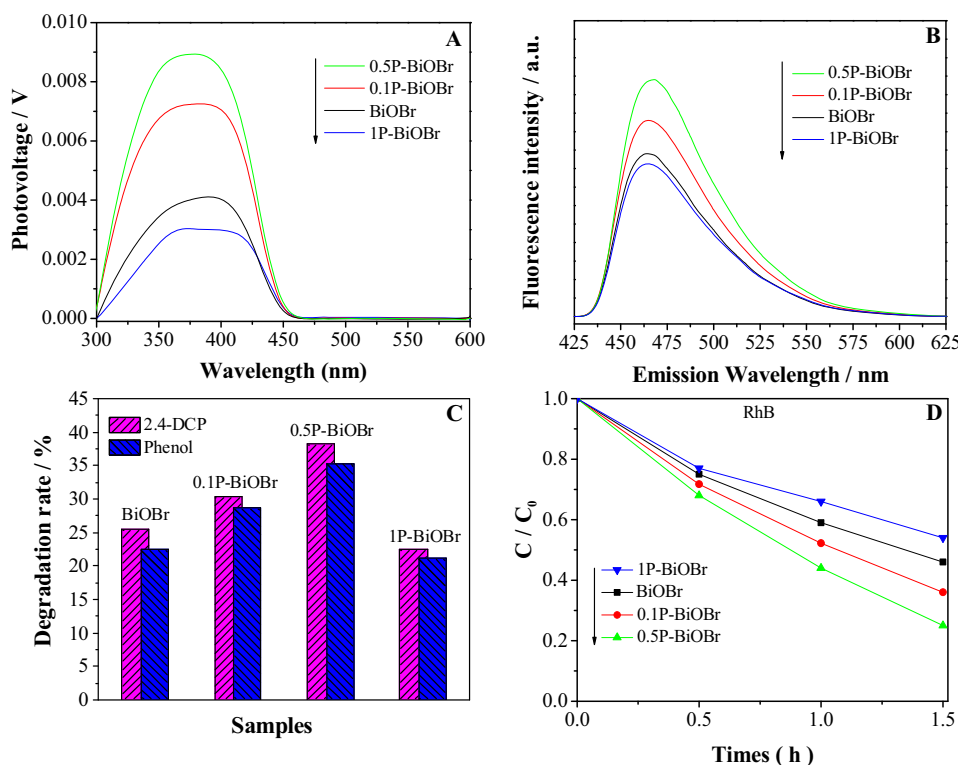
Fig. 1. SS-SPS responses (A), FS spectra related to the amount of •OH radical (B), photocatalytic activities for degrading phenol and 2,4-DCP (C) and rhodamine B (D) of BiOBr, 0.1P-BiOBr, 0.5P-BiOBr and 1P-BiOBr.

semiconducting materials mainly result from the photogenerated charge carrier separation via the diffusion process. In general, the stronger is the SS-SPS response, the higher is the photogenerated charge separation. The SS-SPS responses of BiOBr and XP-BiOBr are shown in Fig. 1A. Obviously, modification with an appropriate amount of hydrogen phosphate greatly enhances the SS-SPS responses of BiOBr. Among the modified BiOBr samples, 0.5P-BiOBr shows the strongest SS-SPS response, indicating the highest charge separation. However, an excess amount of hydrogen phosphate used is unfavorable for charge transportation and separation, consequently leading to the decreased SS-SPS response.

The coumarin fluorescent method applied to determine the amount of hydroxyl radicals (•OH) produced is another vital method to examine the charge separation condition, since the larger is the amount of produced •OH, the more efficient is the separation of photogenerated charges [39]. The fluorescence spectra (FS) related to the produced •OH amount, is shown in Fig. 1B. It could be observed that BiOBr produces a small amount of •OH radical, and the amount of produced •OH is increased with increasing the amount of used hydrogen phosphate. However, the spectrum of 0.5P-BiOBr displays the strongest FS intensity, corresponding to the most efficient charge separation. This is well consistent with the SS-SPS responses.

Hence, it is deduced that the modification with an appropriate amount of hydrogen phosphate could promote the photogenerated charge separation of BiOBr. Thus, it is anticipated that the modification with hydrogen phosphate could improve the photocatalytic activities of BiOBr. Fig. 1C indicates that the photocatalytic activities of the modified BiOBr for degrading phenol and 2,4-DCP are much higher than that of the BiOBr, and the 0.5P-BiOBr exhibits the best photocatalytic performance. However, an excess amount of hydrogen phosphate as modifier would reduce the photocatalytic activity. Thus, it is confirmed that the photocatalytic activities of modified BiOBr depend on the photogenerated charge separation.

To further confirm the enhanced photocatalytic activities, we have also measured the photocatalytic degradation of rhodamine B, as shown in Fig. 1D. It is shown that the photocatalytic activity of 0.5P-BiOBr sample is the best among the modified ones. Therefore, it is concluded that the improved photocatalytic activity of BiOBr after modification with hydrogen phosphate is mainly attributed to the enhanced photogenerated charge separation. To further support the above results, we have recorded electrochemical reduction curves of O_2, as shown in Fig. 2A. One can see that the O_2-redcution current of BiOBr could be obviously increased after the modification with a proper amount of hydrogen phosphate. Among the modified BiOBr, the observed current is the highest for the 0.5P-BiOBr. From the inset of Fig. 2A, one can see that the samples exist two desorption peaks, and the desorption peaks at 300 and 500 °C respectively represent the physical and chemical adsorption of O_2. It is naturally deduced that the enhanced chemical adsorption is useful for effective charge transfer to adsorbed O_2. The modified BiOBr samples, especially for the 0.5P-BiOBr, exhibit stronger O_2-TPD signals than the un-modified one. The strong TPD signal implies the high-amount desorbed O_2 [32]. The results confirm that the capacity of BiOBr to adsorb O_2 could be remarkably increased by the modification with a proper amount of hydrogen phosphate [33]. However, it is unfavorable for O_2 adsorption if the amount of modified hydrogen phosphate is in excess. This possibly is attributed to its aggregation at high concentration. Hence, it is deduced that the modification with hydrogen phosphate could increase the adsorption of O_2 so as to promote the photogenerated electrons captured by the adsorbed O_2, further leading to the enhanced charge separation.

According to the above discussion, a possible mechanism is suggested, as depicted in Fig. 2B. After a proper amount of hydrogen phosphate is modified on the surface of BiOBr, the ability to adsorb O_2 is greatly increased. The increased amount of absorbed O_2 could facilitate the capture of photogenerated electrons, resulting in the
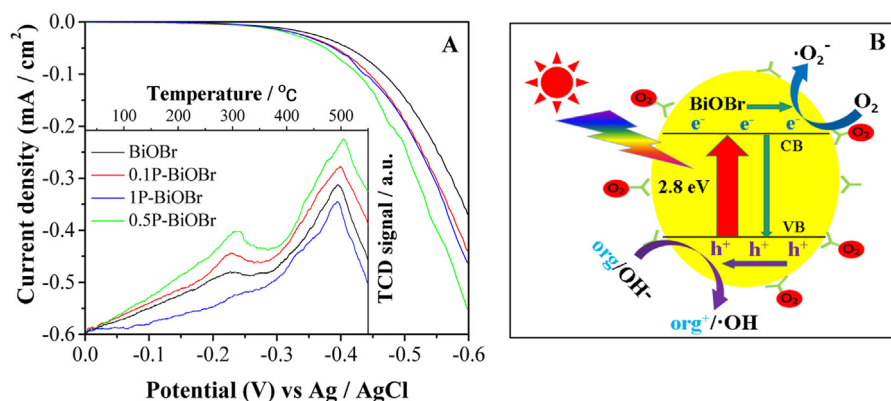
Fig. 2. Electrochemical reduction curves of O_2 (A) with the O_2-TPD curves as the inset of BiOBr, 0.1P-BiOBr, 0.5P-BiOBr and 1P-BiOBr, and a mechanism schematic of hydrogen phosphate-modified BiOBr for the photogenerated charge transfer and separation and induced photocatalytic processes (B).

enhanced charge separation. As a result, the photocatalytic activities for degrading phenol, 2,4-DCP and rhodamine B have been markedly improved. In addition, the formed negative fields after modification with hydrogen phosphate in water could trap positive holes so as to promote the charge separation, which is also favorable for the photocatalytic degradation of liquid-phase pollutants [40].

3.2. Effects of modification with bismuth phosphate

To investigate the surface composition and chemical states of the elements, XPS measurements of pristine BiOBr, 0.5P-BiOBr, and 0.3PP-BiOBr samples are performed, as shown in Fig. 3. In Fig. 3A, the O1s spectra of all the three samples show the main peaks at around 530.1 eV, which are assigned to the lattice oxygen [41]. The peaks at 68.6 and 69.5 eV are respectively associated with $Br3d_{5/2}$ and $Br3d_{3/2}$ (Fig. 3B). The peaks at 159.6 and 164.9 eV are observed (Fig. 3C), respectively correspond to the $Bi4f_{7/2}$ and $Bi4f_{5/2}$ of Bi^{3+} in BiOBr [42]. Compared with the pure BiOBr, the binding energy of Bi4f in 0.3PP-BiOBr is slightly shifted toward the higher energy side, indicating that a new chemical state of Bi by BiPO4 is formed [41,42]. In comparision, it is nearly unchanged for the binding energy of Bi4f in 0.5P-BiOBr. The XPS spectrum of P2p (0.92%) in 0.3PP-BiOBr (Fig. 3D) exhibits a broad band at about 132.5 eV, which is often ascribed to the PO_4^{3-} group in the phosphate compounds [41]. Based on the Bi4f and P2p spectra, it is inferred that the bismuth phosphate has been successfully modified on the surfaces of BiOBr. Whereas, the XPS peak of P2p (0.5%) at about 133.2 eV in 0.5P-BiOBr sample indicates that the hydrogen phosphate has been modified on BiOBr [32].

However, as indicated by the XRD patterns of BiOBr and XPP-BiOBr (SI-Fig. 2A), the crystal phase of BiOBr remains unchanged after introducing the bismuth phosphate. In addition, no characteristic peaks of bismuth phosphate are observed, which is possibly because the tiny amount of formed bismuth phosphate dispersed uniformly on BiOBr. The DRS spectra shown in SI-Fig. 2B demonstrate that the optical absorption of BiOBr stays unchanged after bismuth phosphate modification.

According to the SEM images in SI-Fig. 3, the pristine BiOBr possesses a plate-like morphology with nano-sized thickness, and its morphology is unchanged after the either type of phosphate modification. In order to further investigate the structure of BiOBr, 0.5P-BiOBr and 0.3PP-BiOBr, the TEM and HRTEM images were taken as shown in Fig. 4. The pure BiOBr (Fig. 4A) and 0.5P-BiOBr (Fig. 4B) exhibit a nanoplate structure with smooth surface. However, there exist some ultrafine nanoparticles on the surface of 0.3PP-BiOBr (Fig. 4C). Notably, combining with the XPS results

of 0.3PP-BiOBr, the formed nanoparticles with ∼4 nm diameter are identified to be bismuth phosphate, which are uniformly dispersed on the surface of BiOBr respectively, nanoplates. As shown in Fig. 4D, the lattice fringes of 0.2628 and 0.212 nm correspond to the (111) plane of BiOBr and to the (211) plane of monoclinic BiPO4, respectively. Therefore, it is deduced that the BiPO4 nanoparticles are uniformly grown in situ on the surfaces of BiOBr via a simple wet-chemical method. Hence, it is confirmed that an intimate contact exists between BiPO4 and BiOBr.

The FS spectra related to the produced •OH amounts on XPP-BiOBr samples are shown in Fig. 5A. Obviously, the 0.3PP-BiOBr sample exhibits a strong FS signal, indicating a highly efficient charge separation. It is well known that, when electron-hole pairs are generated in the space charge region of a semiconductor particle, they immediately separate under the built-in electric field, leading to a fast SPV component ($<10^{-5}$ s). Besides the built-in electric field, the charge separation is influenced by the carrier diffusion process, mainly contributing to a slow photovoltage response ($>10^{-4}$ s) [33]. It is expected that in air atmosphere, since the presence of adsorbed O_2 is favorable to capture photogenerated electrons, so that the holes on the surface will produce a positive signal via the carrier diffusion process [33]. As shown in Fig. 5B, the TS-SPV response of BiOBr is greatly increased after modification with the hydrogen phosphate and the bismuth phosphate. Moreover, the photogenerated charge carrier lifetime is also prolonged. Obviously, the enhanced TS-SPV response and prolonged carrier lifetime indicate the promoted photogenerated charge separation, and the positive effects of 0.3PP-BiOBr are more significant than those of 0.5P-BiOBr.

The photocatalytic activities of XPP-BiOBr have been investigated for phenol and 2,4-DCP degradation and relevant results are shown in Fig. 5C. 0.3PP-BiOBr exhibits the highest photocatalytic activities among all XPP-BiOBr samples. The photocatalytic activities of XPP-BiOBr samples are also measured for the degradation of rhodamine B (Fig. 5D). The photocatalytic activity of 0.3PP-BiOBr is higher than any other samples. In addition, 0.3PP-BiOBr shows better photocatalytic activities than 0.5P-BiOBr, indicating the advantage of BiPO4 modification strategy. In addition, it is shown that the stabilities of 0.5P-BiOBr and 0.3PP-BiOBr are good to keep unchanged photocatalytic activities after 3-run recyclable experiments, while that of unmodified BiOBr is a little weak. This improved stability is mainly attributed to the modified phosphate species. Notably, the evaluated photocatalytic activities are consistent with the corresponding charge separation situation.

The question haunts that what actually leads to the enhanced charge separation of BiOBr after bismuth phosphate modification. Is it similar to the hydrogen phosphate modification? To find the
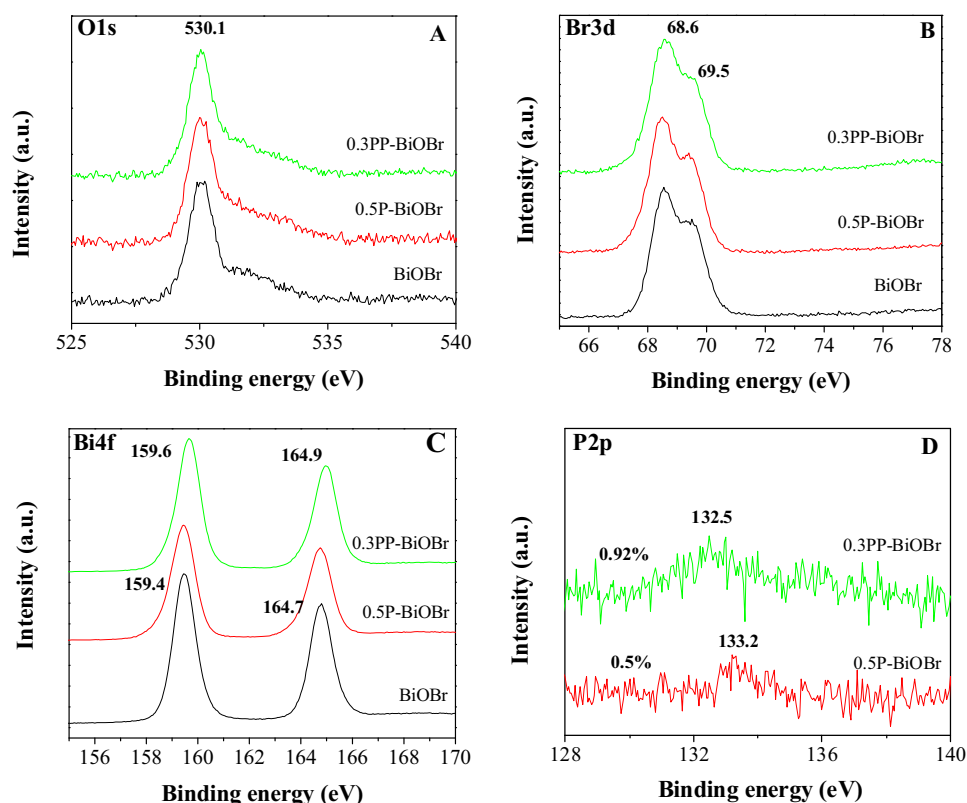
Fig. 3. XPS spectra of BiOBr, 0.5P- BiOBr and 0.3PP- BiOBr: (A) O1s, (B) Br3d, (C) Bi4f and (D) P2p.
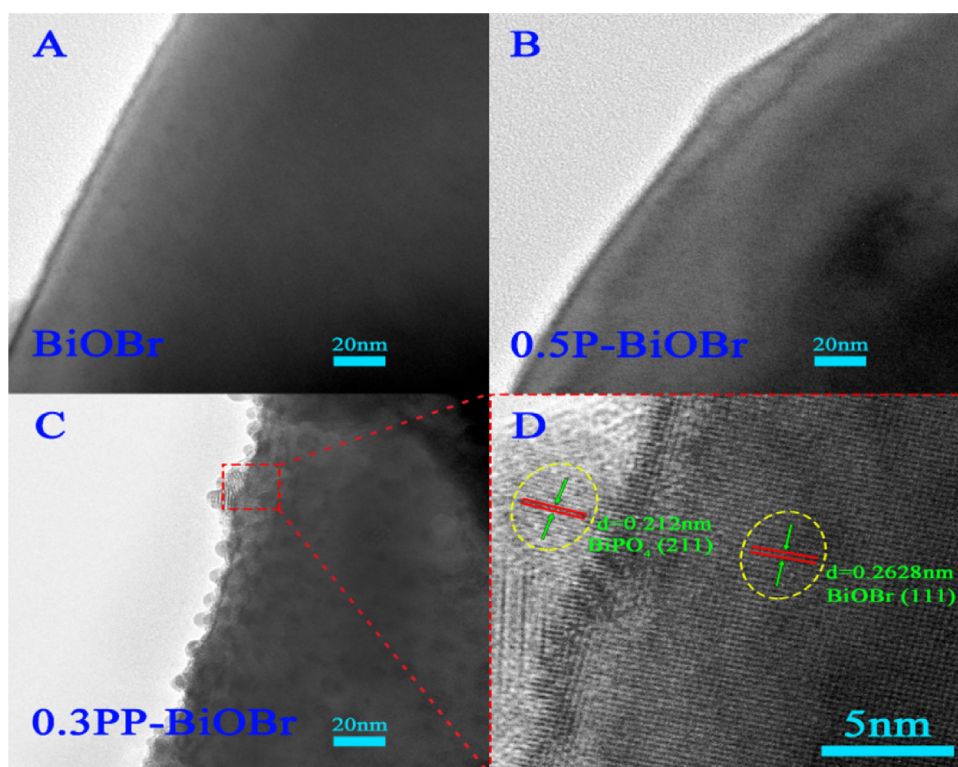

Fig. 4. TEM images of BiOBr (A), 0.5P-BiOBr (B) and 0.3PP-BiOBr (C), and HRTEM image of 0.3PP-BiOBr (D).

answer, we have first tested O_2-TPD curves (SI-Fig. 4), and the result shows that the capacity of BiOBr to adsorb O_2 is not enhanced after modification with bismuth phosphate. Thus, it is deduced that there

should be a different modification mechanism from the promoted adsorption of O_2. Moreover, we have measured the atmosphere controlled SS-SPS responses (SI-Fig. 5), it is noticed that, as the oxy-
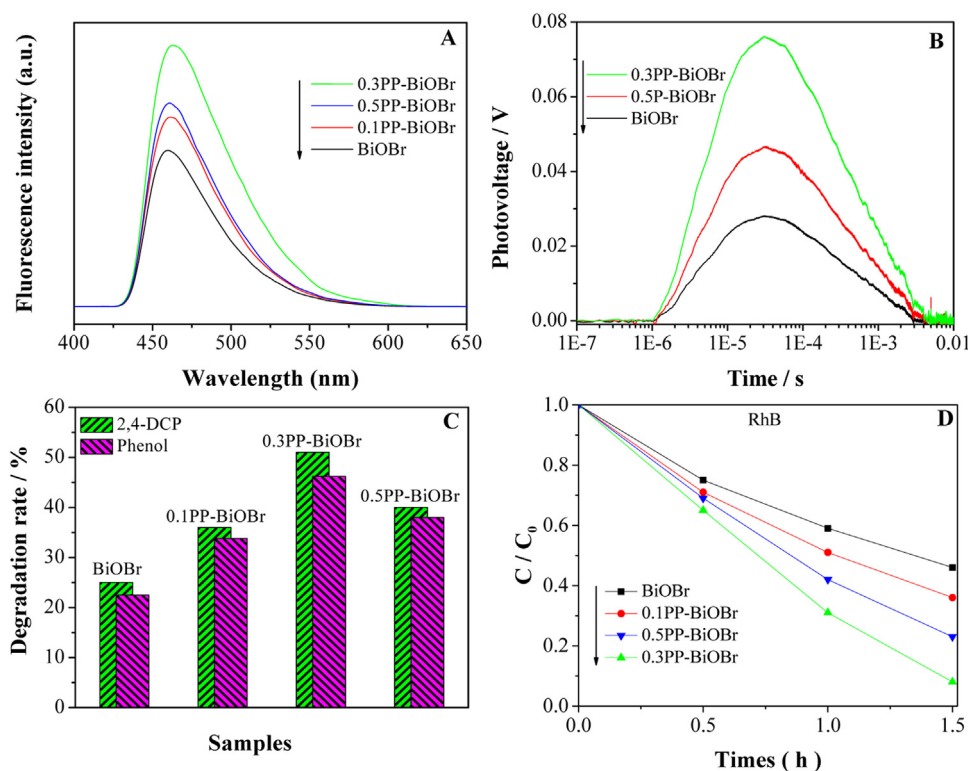
Fig. 5. FS spectra related to the •OH amount (A), TS-SPV responses (B), photocatalytic activities for degrading phenol and 2,4-DCP (C), and rhodamine B (D) of different samples.
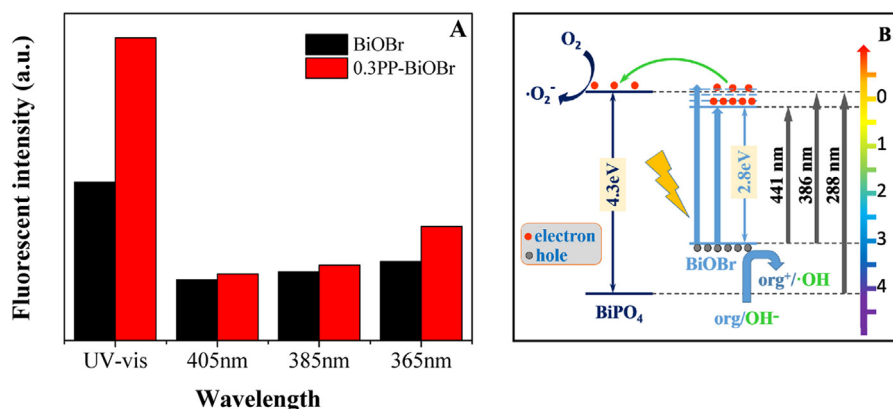

Fig. 6. FS intensities related to the •OH amounts vs different excitation wavelengths of BiOBr and 0.3PP-BiOBr (A), and the mechanism schematic for charge transfer and separation and the induced reactions on $BiPO_4$-modified BiOBr (B).

gen content increases, the SS-SPS signal becomes strong gradually. What's more, the bismuth phosphate modified sample shows an obvious SS-SPS response in N_2. This indicates that the SPS signal of modified sample originates from the charge transfer from BiOBr to $BiPO_4$, as well as from the adsorbed O_2 to capture photogenerated electrons [26]. To further explore the reasons of enhanced charge separation, the FS intensities related to the •OH amount vs different excitation wavelength of BiOBr and 0.3PP-BiOBr were studied, as shown in Fig. 6A. For BiOBr, the FS intensity gradient keeps a relative-smooth variation with decreasing the excitation wavelength. However, for 0.3PP-BiOBr the FS intensity is greatly enhanced at 365 nm, which is attributed to the electron immigration from BiOBr to $BiPO_4$, mainly depending on the excitation wavelength.

Based on the above results, along with the energy band structures [17,43], a schematic on the processes of charge transfer and separation and the induced reactions is suggested, as shown in Fig. 6B. It is illustrated that the electrons from the VB of BiOBr could be excited to the different energy-level of CB under light irradiation, including high-energy region (above −0.16 eV) and low-energy one (from +0.2 eV to −0.16 eV). As for the photogenerated electrons at the low-energy level, they would relax rather fast to the CB bottom and then recombine with holes in the VB. Differently, the partially excited HEL electrons could thermodynamically transfer to the CB of $BiPO_4$, leading to the enhanced charge separation.

Therefore, it is concluded that the photogenerated charge separation of BiOBr could be enhanced after modulating electrons by modifying respectively with the hydrogen phosphate and the bismuth phosphate with different enhancement mechanisms, resulting into the greatly improved photoactivities, especially for the latter. Since it is the case, the formed intermediate, •O_2^-, as the
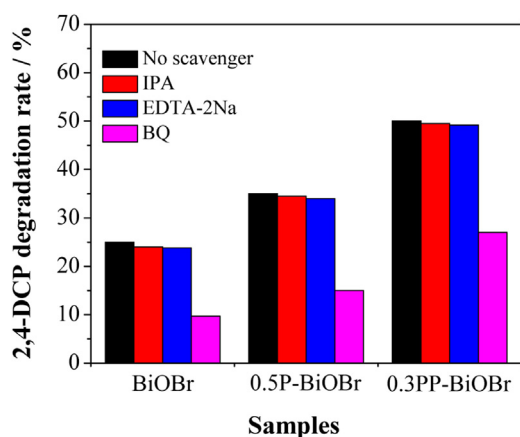
Fig. 7. Photocatalytic degradation rates of 2,4-DCP in the presence of IPA, BQ and EDTA-2Na after irradiation for 1 h over different samples.

electron-modulation production, should play an important role in the degradation of pollutants.

3.3. Degradation mechanism and sequential pathway

Generally, the superoxide radicals ($\cdot O_2^-$), $\cdot OH$ and active holes (h^+) are considered to be responsible for the effective photodegradation of organic pollutants. To gain a more in-depth recognition about the photocatalytic mechanism in this study, isopropanol (IPA), benzoquinone (BQ) and ethylenediamine tetraacetic acid disodium salt (EDTA-2Na) have been used as scavenging species in order to investigate the generation and roles of $\cdot OH$, $\cdot O_2^-$ and h^+, respectively [44]. A series of experiments are carried out to examine the effects of different reactive species on the photodegradation rate of 2, 4-DCP. As shown in Fig. 7, with 1 mM of IPA added to the system of BiOBr, 0.5P-BiOBr, 0.3PP-BiOBr, respectively, the degradation rate of 2,4-DCP does not change obviously, and similar results also happened in the presence of EDTA-2Na. However, when 1 mM of BQ is used, the degradation of 2,4-DCP is strongly inhibited, suggesting that the formed $\cdot O_2^-$ is the main active specie involved

in the degradation of 2,4-DCP on BiOBr, 0.5P-BiOBr and 0.3PP-BiOBr, whereas $\cdot OH$ and h^+ are not the crucial catalytic species in the degradation.

To further clarify the degradation mechanism, we have carried out the analyses of the intermediates formed during 2,4-DCP degradation over 0.3PP-BiOBr by liquid chromatography tandem mass spectrometry and ion chromatography. All the mass spectra of the intermediates are shown in SI-Fig. 6A-E. Based on the detected intermediate results, a possible photodegradation pathway of 2,4-DCP over 0.3PP-BiOBr is illustrated in Scheme 1. It is obvious that the $\cdot O_2^-$ would directly attack the aromatic ring and remove a single Cl^- as the first key step to form parachlorophenol superoxide radical (m/z value of 159.5) [45]. The 159.5 signal is further supported by the LC–MS/MS with Product Ion mode as the inset in SI-Fig. 6A. It is deduced that the observed 2-hydroxy-1,4-benzoquinone ($m/z = 123$), and 4-chlorocyclopenta-1,3-dien-1-ol ($m/z = 115$) result from the fragments of 159.5.

In the second step, 4-chlorocatechol ($m/z = 143.5$, as shown SI-Fig. 6B) is subsequently produced [45]. As for the process of removing the second Cl^-, $\cdot O_2^-$ would directly attack and then produce 1,2-benzenediol superoxide radical according to the detected m/z value of 141 (SI-Fig. 6C). The amount of productions detected during the LC-MS/MS analysis after different time intervals are shown in SI-Fig. 7. One can notice that the intensities of the peaks with m/z values of 159.5 and 143.5 increase with increasing the irradiation, and then keep unchanged or go down, suggesting that it is difficult to be further degraded. In addition, the intensity of the peak with m/z value of 141 increases continuously with the irradiation time increase from 0.5 to 1.5 h, suggesting that the 1,2-benzenediol superoxide radical is much difficult to be further degraded to 1,2,4-benzenetriol ($m/z = 125$, as shown SI-Fig. 6D). The degradation of 1,2-benzenediol superoxide radical to 1,2,4-benzenetriol is more difficult than that of the parachlorophenol superoxide radical to 4-chlorocatechol. It is because the polarity of $\cdot OH$ is larger than the polarity of Cl^-. In the process of superoxide radical conversion to phenolic hydroxyl, the repulsive force of para-position $\cdot OH$ is more obvious. Then, 1,2,4-benzenetriol is attacked by $\cdot OH$ to generate maleic acid ($m/z = 115$, as shown SI-Fig. 6E) and oxalic acid ($m/z = 89$, as shown SI-Fig. 6F). Obviously, the concentration of
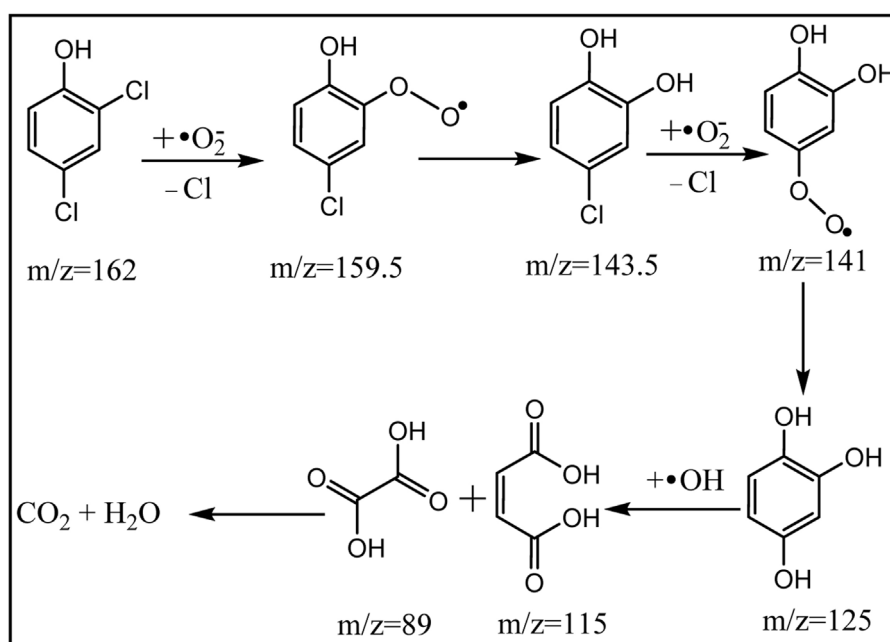
Scheme 1. Proposed pathway for 2,4-DCP degradation on 0.3PP-BiOBr photocatalyst.

maleic acid increase from 0.5 h to 1.5 h, indicating the maleic acid is relatively difficult to be further degraded, due to its structure stability of maleic acid and the block of its two •OH [46].

In the end, the middle production is totally converted into mineral substances, like CO_2 and H_2O. In order to confirm the dechlorination process, the chloride ion concentration is measured with the help of ion chromatography technique. The mineralized chloride amounts of 0.3PP-BiOBr photocatalyst at different period are shown in SI-Fig. 8. The dechlorination of 2,4-DCP gradually increases as the irradiation time is prolonged. At 0.5 h, 0.88 mg/L of chloride is detected, which is reasonable relative to the theoretical result (0.72 mg/L) for removing single chloride at 33.3% degradation rate. When the irradiation time is 2.5 h, 4.32 mg/L of chloride is produced, which is in good agreement with the theoretical results (4.36 mg/L) for removing double chloride at 100% degradation rate. Hence, it is demonstrated that it is a rather slow process to remove Cl^-, especially for the second Cl^-, and the formed $•O_2^-$ would play an important role in the dechlorination of 2,4-DCP.

4. Conclusions

In this work, we have successfully developed the strategy of the modification with the molecular hydrogen phosphate groups and the bismuth phosphate nanoparticles to greatly increase the separation and the lifetime of photogenerated charges of resulting BiOBr nanoplates, especially for the bismuth phosphate one, leading to the obviously improved photocatalytic activities for 2,4-DCP pollutant. It is confirmed that the modified hydrogen phosphate could enhance the adsorption of O_2 so as to promote the electrons captured, while the modified bismuth phosphate could collect the excited high-energy-level electrons from BiOBr, which are responsible for the enhanced charge separation. Moreover, it is expectedly proved that the formed $•O_2^-$ species could dominate the photocatalytic degradation of 2,4-DCP. Furthermore, the possible degradation mechanism related to $•O_2^-$ attack is proposed. Naturally believed, the developed strategy of modulating the photogenerated electrons for the enhanced charge separation and hence for the efficient photocatalysis to degrade organic pollutants on BiOBr is highly feasible and effective, especially for the chlorophenols. This is also applicable to other bismuth oxyhalide photocatalysts for environmental remediation.

Acknowledgements

Appendix A. Supplementary data

Supplementary data associated with this article can be found, in the online version, at http://dx.doi.org/10.1016/j.apcatb.2017.03.003.

References

[1] M. Pera-Titus, V. Garcıa-Molina, M.A. Banos, J. Gimenez, S. Esplugas, Appl. Catal. B-Environ. 47 (2004) 219–256.
[2] D.F. Ashwana, L.L. Sarah, E.S. Michael, L.B. Donna, Environ. Sci. Technol. 48 (2014) 14300–14308.
[3] L.F. Yin, Z.Y. Shen, J.F. Niu, J. Chen, Y.P. Duan, Environ. Sci. Technol. 44 (2010) 9117–9122.
[4] C. Serge, M. Claudio, V. Davide, Environ. Sci. Technol. 41 (2007) 3127–3133.
[5] J. Xu, Z. Cao, X. Liu, H. Zhao, X. Xiao, J.P. Wu, X.H. Xu, J.L. Zhou, J. Hazard. Mater. 317 (2016) 656–666.
[6] Z.P. Cao, M.H. Zhang, J.L. Zhang, H.W. Zhang, Bioresour. Technol. 212 (2016) 138–143.
[7] Z.F. Bian, F.L. Cao, J. Zhu, H.X. Li, Environ. Sci. Technol. 49 (2015) 2418–2424.
[8] H.H. Wang, J. Yang, Y.Y. Liu, S.Y. Song, J.F. Ma, Cryst. Growth Des. 15 (2015) 4986–4992.
[9] X.Y. Fan, K.R. Lai, L.C. Wang, H.S. Qiu, J. Yin, P.J. Zhao, S.L. Pan, J.B. Xu, C.Y.J. Wang, Mater. Chem. A 3 (2015) 12179–12187.
[10] X.M. Tu, S.L. Luo, G.X. Chen, J.H. Li, Chem. Eur. J. 18 (2012) 14359–14366.
[11] H. Li, J. Shang, Z.H. Ai, L.Z. Zhang, J. Am. Chem. Soc. 137 (2015) 6393–6399.
[12] C. Zhang, Y.F. Zhu, Chem. Mater. 17 (2005) 3537–3545.
[13] W.L. Huang, Q.S. Zhu, Comput. Mater. Sci. 43 (2008) 1101–1108.
[14] L. Wang, T.F. Jia, X. Yan, C.H. Li, L.J. Feng, Catal. Today 264 (2016) 257–260.
[15] Y.Y. Yin, Q. Liu, D. Jiang, X.J. Du, J. Qian, H.P. Mao, K. Wang, Carbon 96 (2016) 1157–1165.
[16] Y.X. Guo, Y.H. Zhang, N. Tian, H.W. Huang, ACS Sustainable Chem. Eng. 4 (2016) 4003–4012.
[17] L.Q. Jing, Y. Cao, H.Q. Cui, J.R. Durrant, J.W. Tang, D.N. Liu, H.G. Fu, Chem. Commun. 48 (2012) 10775–10777.
[18] Y. Cao, L.Q. Jing, X. Shi, Y.B. Luan, J.R. Durrant, J.W. Tang, H.G. Fu, Phys. Chem. Chem. Phys. 14 (2012) 8530–8536.
[19] J.W. Tang, J.R. Durrant, D.R. Klug, J. Am. Chem. Soc. 130 (2008) 13885–13891.
[20] L.Q. Jing, J. Zhou, J.R. Durrant, J.W. Tang, D.N. Liu, H.G. Fu, Energy Environ. Sci. 5 (2012) 6552–6558.
[21] D. Yuan, L.Y. Huang, Y.P. Li, Y.G. Xu, H. Xu, S.Q. Huang, J. Yan, M.Q. He, H.M. Li, RSC Adv. 6 (2016) 41204–41213.
[22] Y.A. Ilan, G. Czapski, D. Meisel, Biochim. Biophys. Acta 430 (1976) 209–224.
[23] M.G. Walter, E.L. Warren, J.R. McKone, S.W. Boettcher, Q.X. Mi, E.A. Santori, N.S. Lewis, Chem. Rev. 110 (2010) 6446–6473.
[24] J. Wu, H.Q. Cui, X.L. Zhang, Y.B. Luan, L.Q. Jing, Phys. Chem. Chem. Phys. 17 (2015) 15837–15842.
[25] Z.J. Li, Y.B. Luan, Y. Qu, L.Q. Jing, ACS Appl. Mater. Interfaces 7 (2015) 22727–22740.
[26] M.Z. Xie, X.D. Fu, L.Q. Jing, P. Luan, Y.J. Feng, H.G. Fu, Adv. Energy Mater. 4 (2014) 1300995.
[27] M. Humayun, A. Zada, Z.J. Li, M.Z. Xie, X.L. Zhang, Y. Qu, F. Raziq, L.Q. Jing, Appl. Catal. B-Environ. 180 (2016) 219–226.
[28] X.D. Fu, M.Z. Xie, P. Luan, L.Q. Jing, ACS Appl. Mater. Interfaces 6 (2014) 18550–18557.
[29] Y.Y. Zhu, Q. Ling, Y.F. Liu, H. Wang, Y.F. Zhu, Appl. Catal. B-Environ. 187 (2016) 204–211.
[30] S. Ganguli, C. Hazra, M. Chatti, T. Samanta, V. Mahalingam, Langmuir 32 (2016) 247–253.
[31] S. Obregon, Y.F. Zhang, G. Colon, Appl. Catal. B-Environ. 184 (2016) 96–103.
[32] J. Jiang, K. Zhao, X.Y. Xiao, L.Z. Zhang, J. Am. Chem. Soc. 134 (2012) 4473–4476.
[33] C. Liu, L.Q. Jing, L.M. He, Y.B. Luan, C.M. Li, Chem. Commun. 50 (2014) 1999–2001.
[34] H. Li, J. Shang, Z.H. Ai, L.Z. Zhang, J. Am. Chem. Soc. 137 (2015) 6393–6399.
[35] J.Y. Liu, Y. Bai, P.Y. Luo, P.Q. Wang, Catal. Comm. 42 (2013) 58–61.
[36] D. Wu, S.T. Yue, W. Wang, T.C. An, G.Y. Li, H.Y. Yip, H.J. Zhao, P.K. Wong, Appl. Catal. B-Environ. 192 (2016) 35–45.
[37] Z. Amir, H. Muhammad, R. Fazal, X.L. Zhang, Y. Qu, L.L. Bai, C.L. Qin, L.Q. Jing, H.G. Fu, Adv. Energy Mater. (2016) 1601190.
[38] R. Fazal, Y. Qu, X.L. Zhang, H. Muhammad, J. Wu, Z. Amir, H.T. Yu, X.J. Sun, L.Q. Jing, J. Phys. Chem. C 120 (2016) 98–107.
[39] H. Wang, Y. Su, H.X. Zhao, H.T. Yu, S. Chen, Y.B. Zhang, X. Quan, Environ. Sci. Technol. 48 (2014) 11984–11990.
[40] M.Z. Xie, J. Bian, H. Muhammad, Y. Qu, Y.J. Feng, L.Q. Jing, Chem. Commun. 51 (2015) 2821–2823.
[41] Z.S. Li, S.Y. Yang, J.M. Zhou, D.H. Li, X.F. Zhou, C.Y. Ge, Y.P. Fang, Chem. Eng. J. 241 (2014) 344–351.
[42] H.P. Li, T.X. Hu, N. Du, R.J. Zhang, J.Q. Liu, W.G. Hou, Appl. Catal. B-Environ. 187 (2016) 342–349.
[43] W.J. An, W.Q. Cui, Y.H. Liang, J.S. Hu, L. Liu, Appl. Surf. Sci. 351 (2015) 1131–1139.
[44] Y.F. Liu, Y.Y. Zhu, J. Xu, X.J. Bai, R.L. Zong, Y.F. Zhu, Appl. Catal. B-Environ. 142 (2013) 561–567.
[45] H.Y. Zhou, S. Qian, W. Xun, L.X. Wang, J. Chen, J.D. Zhang, X.H. Lu, Sep. Purif. Technol. 132 (2014) 346–353.
[46] X.M. Zhang, P. Murria, Y. Jiang, W.H. Xiao, H.I. Kenttamaa, M. Abu-Omarb, N.S. Mosier, Green Chem. 18 (2016) 5219–5229.